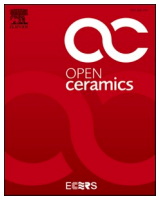
Open Ceramics 26 (2026) 100978



Contents lists available at ScienceDirect

Open Ceramics

journal homepage: www.sciencedirect.com/journal/open-ceramics





Composition and interface stability of sputtered MoO_x ultra-thin films on silicon for optoelectronic applications

Salvatore La Manna [a,*], Vanna Torrisi [a], Giorgia Franzò [a], Cristiano Lo Pò [b], Elisa Brugaletta [c], Antonio Massimiliano Mio [c], Antonio Terrasi [a,b], Guglielmo G. Condorelli [d], Maria Miritello [a]

[a] IMM-CNR, Sede Catania (Università), via S. Sofia 64, 95123 Catania, Italy
[b] Dipartimento di Fisica e Astronomia "Ettore Majorana", Università di Catania, via S. Sofia 64, 95123, Catania, Italy
[c] IMM-CNR, HQ, Z.I. VIII Strada 5, 95121 Catania, Italy
[d] Dipartimento di Scienze Chimiche, Università di Catania, viale A. Doria 6, 95125, Catania, Italy

ARTICLE INFO

Keywords:
Sputtering
Hole-selective layer
Interfacial stability

ABSTRACT

Sub-stoichiometric molybdenum oxide (MoO_x) has attracted significant attention as hole-transport/selective layer in optoelectronic devices. However, its integration on Si is hindered by interfacial redox-reactions that can alter oxide stoichiometry and electronic properties.

In this work, MoO_x films, 5 nm thick, were deposited by non-reactive RF sputtering from a stoichiometric MoO_3 ceramic target onto bare and thermally-oxidized Si substrates. Morphological analyses confirmed the formation of continuous and dense coatings, Kelvin probe mapping revealed spatially uniform WF of 5.06 eV. Angle-resolved XPS showed sub-stoichiometric composition ($x = 2.6$) regardless of substrate, with no variations across the film thickness. These results were corroborated by HAADF-STEM, which revealed uniform Mo and O distributions, confirming the absence of interfacial oxide reactions. Compared to thermally evaporated counterparts, sputtered films exhibit superior compositional stability due to the higher kinetic energy of sputtered species involved in the film growth. Overall, non-reactive sputtering enables the growth of stable films suitable for optoelectronic and photovoltaic applications.

Introduction

Optoelectronic conversion plays a central role in a wide range of technologies that enable the generation, detection, and manipulation of light. The development of next-generation devices increasingly relies on advanced functional materials that serve as key components within complex device architectures. In this context, significant efforts have been devoted to tailoring material properties through strategies such as dimensional control, doping, interface engineering, defect modulation, and structural design. These approaches have enabled the emergence of a broad class of optoelectronic materials, including two-dimensional semiconductors, hybrid perovskites, and transition metal oxides (TMOs), which are widely investigated for applications in photodetection, photovoltaics and sensing [1,2]. TMOs have attracted significant attention in recent years due to their unique combination of tunable electrical, optical, and chemical properties [3,4]. Among them, molybdenum oxide stands out for its remarkable versatility. It is an n-type semiconductor with high melting and boiling points (795 °C and 1155 °C, respectively), a wide bandgap (~3 eV), which guarantees excellent transparency in the visible and infrared regions, and high carrier mobility [5,6]. These features make it highly suitable, particularly in the form of thin or ultra-thin film, for use as hole transport or selective layer in optoelectronic devices, especially in its sub-stoichiometric form (MoO_x), characterized by the presence of lower oxidation states such as Mo^{5+} [3,5,6]. The chemical and physical properties of MoO_x, with $2 < x < 3$, are strongly dependent on its oxidation state and defect chemistry. In particular, its intrinsic redox flexibility, primarily governed by O vacancies, can significantly alter its electronic structure, enabling tunability of electrical conductivity, work function (WF), and optical absorption [7–11]. This tunability makes MoO_x highly attractive for a wide range of applications, including electrochemical storage, photocatalysis, photovoltaics (PV), organic light-emitting diodes, and transistors [3,8,9,12–14]. This is particularly relevant in the broader context of ongoing efforts to develop efficient and stable charge-selective materials for next-generation optoelectronic devices, including silicon heterojunctions, organic photovoltaics and

* Corresponding author.
E-mail address: salvatore.lamanna@dfa.unict.it (S. La Manna).

https://doi.org/10.1016/j.oceram.2026.100978
Received 26 February 2026; Received in revised form 28 April 2026; Accepted 11 May 2026
Available online 12 May 2026
2666-5395/© 2026 Published by Elsevier Ltd on behalf of European Ceramic Society. This is an open access article under the CC BY-NC-ND license (http://creativecommons.org/licenses/by-nc-nd/4.0/).

perovskite-based system [15,16]. Specifically, for silicon-based optoelectronic devices, MoO_x composition and electronic properties play a crucial role in determining band alignment at the interface, directly affecting hole-selective transport properties [17,18]. However, the same redox activity that provides its functional adaptability also poses challenges in terms of chemical stability, especially at interfaces. MoO_x, like other TMOs, exhibits a strong tendency to undergo interfacial redox reactions when in contact with reducing substrates [19,20]. Additionally, its oxidation state and overall composition can evolve upon air exposure, resulting in variations in WF and conductivity [21,22]. Therefore, precise control over oxidation state and stoichiometry, as well as overall structural and chemical stability, becomes critical for device performance, particularly when MoO_x is integrated as ultra-thin layer in electronic or optoelectronic devices [8,9,14,19].

Physical vapour deposition (PVD) techniques are widely adopted to fabricate molybdenum oxide thin films [3,4,8,23]. Among these, thermal evaporation is the most established approach. However, achieving a well-controlled oxide stoichiometry remains challenging due to oxygen loss during film growth. Moreover, it is well-documented that molybdenum oxide films deposited by thermal evaporation onto Si substrates undergo interfacial redox reactions, leading to the formation of a SiO_x interlayer and partial reduction of Mo^{6+} to lower oxidation states (Mo^{5+} or Mo^{4+}) in the near-interface region, in some cases extending up to ~3–4 nm into the film [19,24,25]. These undesirable interfacial reactions hinder reliable stoichiometric control and can significantly alter the optoelectronic properties of the overall oxide layer [26,27]. Sputtering, on the other hand, represents a compelling alternative, particularly for industrial-scale applications, due to its compatibility with automated, high-throughput deposition systems and its ability to produce dense, uniform films with excellent adhesion [28,29]. MoO_x is commonly deposited via reactive sputtering of metallic Mo targets in oxygen-rich atmosphere [3,10]. However, this approach suffers from process instabilities due to target poisoning, which lead to uncontrolled stoichiometry, especially in the ultra-thin regime, where even slight deviations critically affect electronic properties [28,29]. Alternative strategies can involve the use of sub-stoichiometric target[30], or direct sputtering from a stoichiometric MoO_3 ceramic target, which can provide improved process stability and reproducibility [7]. However, despite these potential advantages, these deposition routes remain largely unexplored. To the best of our knowledge, only a few studies have addressed non-reactive sputter-deposited MoO_x films[7,31], and none has systematically investigated their stoichiometry, oxidation states, and interfacial chemistry in the ultra-thin regime (<10 nm), where even small deviations from the desired composition can critically affect device performance.

In this work, we investigate the chemical composition of 5 nm-thick MoO_x films deposited by non-reactive sputtering from a stoichiometric MoO_3 target onto bare and thermally oxidized FZ-Si substrates, with the aim of assessing their stability on silicon platform. Surface morphology was characterized using scanning electron microscopy and atomic force microscopy to establish the formation of continuous and dense coatings despite their reduced thickness. Kelvin probe mapping, performed at micrometric and nanometric scales, were carried out to evaluate uniformity of electronic properties by work function measurements. Angle-resolved X-ray photoelectron spectroscopy and cross-sectional transmission electron microscopy were employed to analyse film stoichiometry, probe depth-dependent oxidation states, and investigate MoO_x/Si interface. Our results demonstrated that sputtered ultra-thin MoO_x films preserve high spatial uniformity in terms of morphology and electronic properties together to high composition integrity on silicon substrate, without evidence of any interfacial reductions arising from substrate-induced redox interactions. This behaviour is particularly significant because it guarantees high stability of optoelectronic properties, not commonly reported for thermally evaporated counterparts. This peculiarity is crucial for maintaining high optical transparency, favourable band alignment, efficient charge-carrier transport, and ultimately improved device performance. Overall, the proposed approach represents as a scalable and reliable route for fabricating stable ultra-thin MoO_x layers suitable for photovoltaics and optoelectronic device applications.

Experimental section

Molybdenum oxide thin films, 5 nm thick, were deposited using an AJA ultra-high vacuum magnetron sputtering system. Depositions were carried out via radiofrequency (RF) sputtering from a 4-inch diameter stoichiometric MoO_3 target (Kurt J. Lesker, purity 99.95%). Sputtering depositions were conducted under an Ar atmosphere at 8.0×10^{-3} mbar, with a radio-frequency (RF) power of 100 W applied to the target. No intentional substrate heating was employed during deposition. Films were simultaneously deposited on two type of 6-inches wafers: (i) n-doped float zone silicon (FZ-Si) substrates (280 μm thick, (100)-oriented, double-side polished, resistivity 1–5 Ω•cm), and (ii) the same FZ-Si substrates coated with a 100 nm-thick thermally grown silicon oxide (SiO_2). Prior to deposition and thermal oxidation, FZ-Si substrates were immersed in a 1–2% (w/v) aqueous HF solution for 2 min to remove the native oxide, followed by drying under N_2 flow. To limit uncontrolled reoxidation, HF-treated substrates were handled under minimized air exposure conditions and transferred into the load-lock of the sputtering system, followed by deposition in a main chamber with a base pressure below 1×10^{-8} mbar. For thermally oxidized substrates, SiO_2 growth was performed in a quartz furnace at 1100 °C for 60 min.

Films thickness was measured using a J. A. Woollam M2000 spectroscopic ellipsometer. Data analysis was performed using Complete EASE software employing a Cauchy dispersion model.

Surface morphology was investigated by scanning electron microscopy (SEM) and atomic force microscopy (AFM). SEM images were acquired using a Carl Zeiss Supra 25 microscope, operating at 5.0 kV in InLens mode with an aperture size of 10 μm. AFM scans were performed in non-contact mode using a Nanosurf Drive AFM system equipped with Bruker SCM-PIT-V2 probes (resonance frequency ~ 75 kHz). Images were collected with 512 × 512 lines at a scan rate of 0.5 Hz. Data processing was carried out using "Gwyddion 2.67″ software, which provided two- and three-dimensional reconstructions and statistical surface parameters such as roughness.

Kelvin Probe Force Microscopy (KPFM) analysis was used to measure the film work function (WF) and KP maps were carried out to evaluate WF on film surface at the nanometric scale. An oscillating potential of 2–3 V at 20 kHz was applied between the conductive tip and the sample simultaneously with morphology acquisition. Surface potential maps were acquired using the second lock-in amplifier of the DriveAFM system, with a bandwidth of 6 kHz. Large-area WF mapping was performed using an APS04 system by KP Technology, equipped with a 2 mm gold-alloy vibrating tip. Measurements were carried out over a 3.42 mm × 3.42 mm area with a scan step of 95.3 μm and a scan rate of 66.8 μm/s. At both length scales, the contact potential difference (V_{CPD}) between the tip and the sample surface was used to calculate the sample WF according to the relation: $WF = V_{CPD} + WF_{Tip}$, *where* WF_{Tip} is the tip WF.

X-ray photoelectron spectroscopy (XPS) was used to investigate film composition and oxidation states using a PHI 5000 VersaProbe II system equipped with a monochromatic Al-Kα source (1486.7 eV), excited by a micro-focused electron beam. Angle-resolved XPS (AR-XPS) measurements were performed to probe film composition and oxidation states with depth-resolution. Photoelectron spectra were acquired at different take-off angles (α = 25°, 45°, and 70°), defined as the angles between the sample surface and the analyser axis, by varying the inclination of the sample holder. Peak deconvolution was carried out using XPS Peak 4.1 software.

High-resolution micrographs and local elemental mapping were performed by scanning transmission electron microscopy (STEM) and Energy-Dispersive X-ray Spectroscopy (EDS). The microscopical analyses have been operated by using a JEOL ARM200F Cs-corrected

microscope, which is equipped with a cold-field emission gun and operating at 200 keV. Micrographs were acquired in Z-contrast mode by high-angle annular dark field (HAADF). A JEOL Centurio, with a 100 mm^2 SDD detector, was used for EDS measurements, through Gatan DigitalMicrograph software, in spectrum imaging (SI) mode.

Cross-sectional TEM lamellae were prepared by focused ion beam (FIB) milling in a Thermo Scientific™ Helios™ 5 UC DualBeam system using 30 keV Ga^+ ions, followed by low-energy (2 keV Ga^+) polishing to minimize FIB-induced amorphization.

Results and discussion

Ultra-thin molybdenum oxide (MoO_x) films were deposited via RF non-reactive sputtering from a stoichiometric molybdenum trioxide (MoO_3) target in a pure Ar atmosphere. Depositions were carried out simultaneously on FZ-Si and thermally oxidized FZ-Si substrates. Deposition conditions were optimized to ensure a stable plasma and a controlled growth rate of 0.9 nm/min, enabling the reproducible fabrication of films with a nominal thickness of 5 nm. Spectroscopic ellipsometry confirmed the target thickness for both substrates. Thickness measurements performed at multiple positions across the 6-inch wafer showed variations within ±4%, indicating a high degree of thickness uniformity over the sampled areas.

Morphological analysis based on plan-view SEM images acquired at different magnifications was used to assess the uniformity and continuity of the deposited films, which is a critical requirement at such low thicknesses. **Figure S1** shows a magnified view of the film surface, revealing a uniform, finely granular surface morphology with no observable voids, cracks, or discontinuities, indicating a continuous and well-adhered ultra-thin films. These observations are fully corroborated by atomic force microscopy (AFM) measurements. The two-dimensional AFM topographic image acquired over a 1 μm × 1 μm area shown in Fig. 1(a), together with the corresponding three-dimensional reconstruction and a representative line profile, reported in **Fig. S2(a)** and **(b)**, respectively, confirmed the smooth and homogeneous nature of the film surface, characterized by a finely textured morphology. The surface roughness, σ, defined as the root mean square (RMS) variation of the height profile, was calculated according to Eq. (1):

$$\sigma = \left[\frac{1}{N}\sum_{i=1}^{N}(Z_i - Z_m)^2\right]^{1/2} \quad (1)$$

where N is the number of data points, Z_i is the height of the individual point, and Z_m is the mean surface height. The estimated RMS roughness was only 0.22 nm, a value consistent with a dense and continuous layer.

Taken together, SEM and AFM results demonstrate that the sputtered ultra-thin films formed a conformal coating, which is essential for photovoltaic and optoelectronic applications requiring uniform functional layers at the nanometer scale.

To investigate the electronic properties of MoO_x ultra-thin film at the nanometric scale, Kelvin probe force microscopy (KPFM) measurements was performed using the same equipment. KPFM image shown in Fig. 1 (b), depicts the surface potential map acquired over the same 1 μm × 1 μm scanned area. Contact potential difference (CPD) remains uniform across the entire observed area, with a total variation of approximately 46.0 mV and a standard deviation of ±5 mV, as indicated by the colour scale bar. The average work function (WF), estimated from these measurements was 5.1 eV, with an excellent lateral uniformity at nanometric scale.

To extend the analysis to larger length scales, spatially resolved KP measurements were carried out using a different KP system based on the off-null detection method. This approach improves measurement accuracy by minimizing the influence of laboratory noise, stray capacitance, and interference from probe vibration frequency and its harmonics [32]. The average CPD, obtained from multiple measurement points across the film surface, was +430 ± 20 mV relative to the tip, corresponding to a WF of 5.06 ± 0.02 eV, in excellent agreement with the nanometric-scale KPFM results. The WF spatial distribution was remarkably uniform, as clearly shown in the *2D WF map* acquired over a 3.0 mm × 3.0 mm area, reported in Fig. 2(a), where X and Y axes represent the scanned lateral position on the film surface and the colour scale corresponds to the measured WF values. This representation reveals that the WF values remain confined within a narrow range between 5.04 eV and 5.08 eV. The higher CPD variation observed at the nanoscale (~46 mV) is mainly attributed to measurement conditions, in particular the reduced tip-sample distance required to resolve the extremely smooth surface morphology, which enhances tip-sample interactions and increases noise in the KPFM signal. In contrast, macroscopic Kelvin probe measurements (Fig. 2) show significantly lower variation, confirming an excellent large-area uniformity of the films.

For comparison, Fig. 2(b) also includes the 2D WF map of the MoO_x film deposited on a thermally oxidized FZ-Si substrate, which exhibits an average WF value of 5.04 ± 0.02 eV. The two samples exhibit comparable WF values within experimental uncertainty and a similar degree of spatial uniformity, with no appreciable differences between films grown on FZ-Si and SiO_2/FZ-Si substrates. Thus, the excellent WF homogeneity, at both nanometric and micrometric scales, confirms the uniformity of the electronic properties across the film surface independently of the underlying substrate. Moreover, the stability of the WF under ambient conditions was further assessed by repeating the measurements monthly

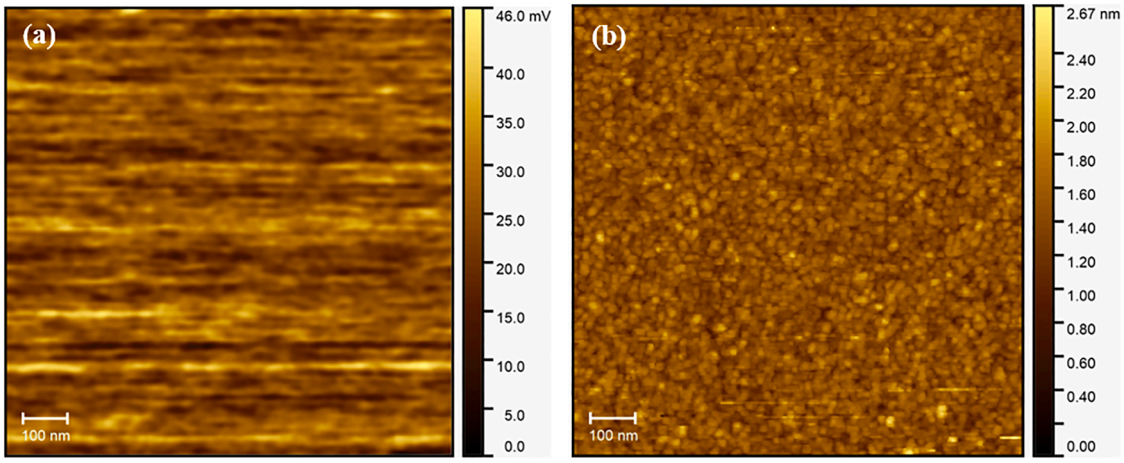


Fig. 1. Two-dimensional AFM topographic image **(a)** and KPFM contact potential difference (CPD) map **(b)** of a 5 nm thick sputter-deposited MoO_x film on FZ-Si, acquired over a 1 μm × 1 μm area.

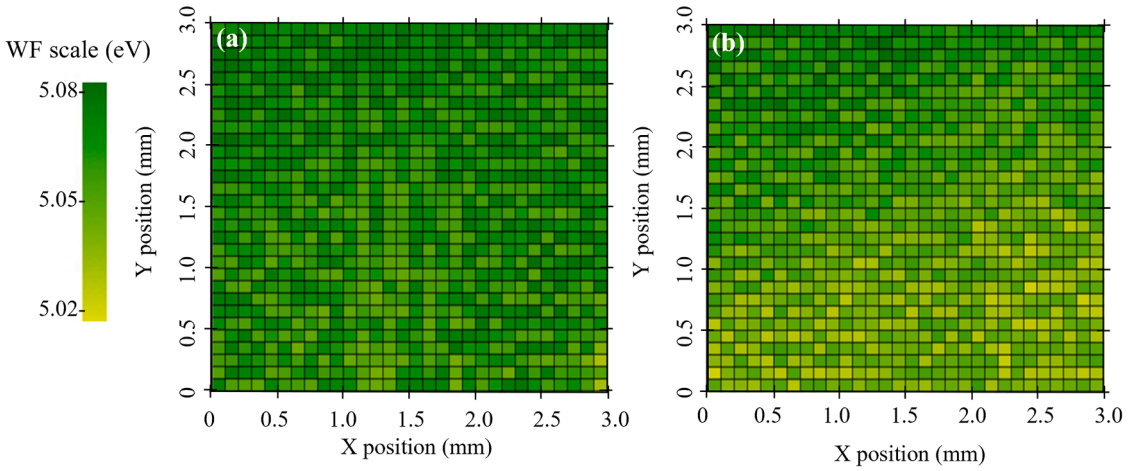


Fig. 2. 2D work function (WF) maps for sputter-deposited molybdenum oxide films acquired over a 3.0 mm × 3.0 mm area: (a) film grown on FZ-Si substrate and **(b)** film grown on thermally oxidized SiO_2/FZ-Si substrate.

over a period of 6 months, with the samples stored under controlled environmental conditions (temperature 25 °C and relative humidity 40%). No significant variations were observed, with WF values remaining unchanged within the experimental uncertainty, indicating good environmental stability of the films.

Although the measured values may appear lower compared to the expected intrinsic WF of stoichiometric MoO_3, typically exceeding 6 eV, it is well established that WF measurements performed under ambient conditions are strongly affected by surface adsorption phenomena [21,22]. In particular, a reduction of approximately 1 eV after air exposure has been reported due to chemisorption of oxygen and moisture on the film surface [21,22]. Accordingly, sub-stoichiometric MoO_x films commonly exhibit WF values in the range of 4.9–5.7 eV following air-exposure [21,22,31,33,34]. The WF values measured ex situ for the sputtered films investigated in this work therefore fall well within the expected range. On this basis, the intrinsic WF of the as-deposited MoO_x films can be reasonably inferred to be close to 6 eV. Such values are well suited for optoelectronic applications, where MoO_x layers are typically integrated within device stacks and capped by adjacent functional layers, effectively preventing direct air-exposure. Previous experimental studies and numerical simulations have shown that MoO_x WF values in the range of ~ 4.8–5.6 eV can effectively operate as hole-selective contacts in silicon-based devices [17]. In particular, a critical threshold is typically identified around ~5.1 eV: below this value, insufficient band bending may lead to the formation of a barrier for hole transport, resulting in S-shaped J-V characteristics and reduced device performance, whereas higher WF values promote efficient carrier extraction and favourable band alignment [17]. More quantitatively, WF values above ~5.1 eV have been shown to reduce the hole transport barrier to only a few tens of meV (e.g., ~0.06 eV), enabling quasi-ohmic hole transport, while simultaneously maintaining a large electron barrier (>1 eV), thus ensuring effective carrier selectivity [18]. For WF values approaching ~6 eV, carrier transport can occur via band-to-band or defect-assisted tunnelling, enabling low-resistance hole-selective contacts, with reported improvements in key device parameters such as open-circuit voltage and fill factor [17]. Consequently, intrinsic WF values of 6 eV obtained in this work, together with their high spatial uniformity, align perfectly with the technologically relevant requirements for hole-selective operation in Si-based heterostructure.

To investigate the chemical composition of non-reactive sputtered MoO_x thin films, X-ray Photoelectron Spectroscopy (XPS) was performed. *Mo_{3d}* and *O_{1s}* core levels peaks recorded for films deposited on FZ-Si substrate are presented in Fig. 3(a) and **(b)**, respectively.

The presence of various Mo oxidation states was identified by analysing XPS spectra of *Mo_{3d}* core-level doublet, as shown in Fig. 3(a). The multi-peak deconvolution, performed using standard constraints for *Mo_{3d}* doublet (fixed area ratio of 1.5 and spin-orbit separation of 3.15 eV), revealed the presence of two Mo oxidation states, corresponding to

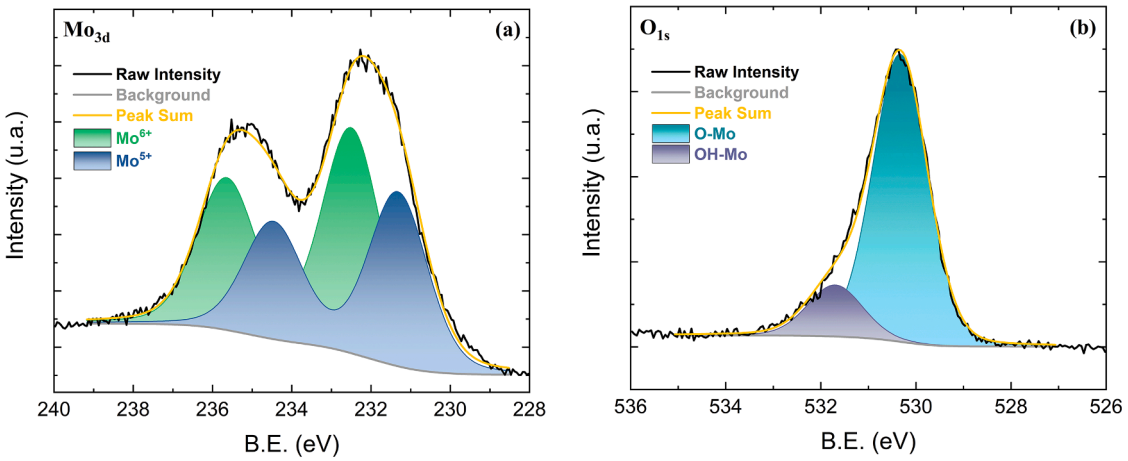


Fig. 3. XPS spectra of Mo_{3d} **(a)** and O_{1s} **(b)** core levels of sputter-deposited molybdenum oxide film grown on FZ-Si. The relative fitting curves are shown as yellow line, they are obtained after Shirley background subtraction (gray line) and the Gaussian–Lorentzian fitting curves of Mo^{6+} (green) and Mo^{5+} (blue) in **(a)**, O-Mo (light blue) and OH-Mo (purple) in **(b)**.

Mo^{6+} and Mo^{5+} cations. The first doublet (green), peaked at binding energies of 232.50 and 235.65 eV, corresponds to the $3d_{5/2}$ and $3d_{3/2}$ levels associated to Mo cations in the higher oxidation state, Mo^{6+} [11,35,36]. The presence of the lower oxidation state, Mo^{5+}, is evident from the other Mo doublet (blue), with $3d_{5/2}$ and $3d_{3/2}$ centred at 231.30 eV and at 234.45 eV respectively [11,35,36]. The main fitting parameters, including $Mo_{3d5/2}$ peak position, Full Width at Half Maximum (FWHM), total Mo_{3d} integrated area, and Lorentzian-Gaussian (L-G) percentage, are summarized in Table 1. XPS peak relative to O_{1s} core level was also recorded and fitted, as shown in Fig. 3(b). The fitting curves revealed two components, a dominant peak (light blue) at 530.30 eV, attributed to lattice oxygen in MoO_x[35,37–40], and a weaker peak (purple) at 531.70 eV, associated to surface -OH groups from atmospheric exposure [35,37,40–42], as commonly observed in MoO_3 and other transition metal oxides [19] Corresponding fitting parameters are listed in Table 1.

The relative percentage of each Mo oxidation state was determined by integrating the area of the corresponding Mo_{3d} components and calculating the ratio between the Mo^{6+} or Mo^{5+} contributions and the total Mo signal. It revealed values of 56% and 44%, respectively, by evidencing a sub-stoichiometric nature of the grown film. In addition, by integrating the total areas of O_{1s} and Mo_{3d} signals, and correcting them for the respective Wagner sensitivity factor[43], the O/Mo atomic ratio was estimated to be 2.6.

The obtained composition supports the WF value obtained from KP measurements, as lower oxidation states of molybdenum are typically associated with reduced WF values [33,34]. The observed sub-stoichiometric composition, despite the use of a stoichiometric MoO_3 target, is likely related to preferential sputtering and differential scattering of O species during RF sputtering, which results in a lower effective O incorporation rate in the growing film [44].

To assess the suitability of sputter-deposited MoOx ultra-thin films for integration into optoelectronic architectures, their environmental stability was investigated. The environmental chemical stability of sputter-deposited MoO_x film was evaluated by XPS analysis. The Mo_{3d} core-level spectra acquired after 3 (t = 1) and 6 (t = 2) months of air exposure retained an identical shape to that recorded immediately after deposition (t = 0), as shown in **Fig. S3**. The absence of spectral changes indicates that the film preserved its stoichiometry and compositional integrity over time, with no detectable oxidation or reduction upon long-term air exposure. These results are consistent with the stable WF values measured over the same time interval, confirming that the electronic properties of the films are not significantly affected by prolonged exposure to ambient conditions.

To evaluate the role of substrate in determining film compositional stability, XPS analysis was carried out by comparing MoO_x film deposited by non-reactive sputtering on FZ-Si and on 100 nm-thick thermally grown SiO_2 layer on FZ-Si substrate. This comparison allows the identification of any substrate-dependent differences in film composition arising from the reducing or oxidized nature of the underlying substrate [19,24,27,45]. The Mo_{3d} spectra of the two films, reported in Fig. 4(a), exhibit nearly identical line shapes. Peak deconvolution confirms the same Mo^{5+} content, equal to 44.0%, in both cases. These findings demonstrate that the chemical composition of sputter-deposited MoO_x film does not exhibit variations regardless of the underlying substrate. This behaviour contrasts with that reported by Tong et al. [24], for thermally evaporated films where the appearance of Mo^{4+} species and an increased Mo^{5+}fraction at the expenses of Mo^{6+} were observed for MoO_x deposited on FZ-Si compared to films grown on a SiO_x layer. Such substrate-dependent features were attributed to redox reactions induced by the reducing nature of bare silicon. The absence of similar evidence in sputtered films suggests that substrate-induced oxide reduction is effectively suppressed under these deposition conditions.

Table 1
Fitting parameters for Mo^{6+} and Mo^{5+} of Mo_{3d} core level and O-Mo and OH-Mo of O_{1s} core level of sputter-deposited molybdenum oxide films grown on FZ-Si. Reported values include peak positions, full width at half maximum (FWHM), total integrated area, and Lorentzian-Gaussian (L-G) percentage.

	Mo_{3d}		O_{1s}	
	Mo^{6+}	Mo^{5+}	O-Mo	OH-Mo
Position	232.50	231.30	530.30	531.70
FWHM	1.76	1.76	1.36	1.36
Area	6834	5290	5016	924
%L-G	22	22	14	14

However, since XPS is a surface sensitive technique, possible interfacial reactions involving only a few nanometers near the silicon interface cannot be excluded. Thus, angle-resolved X-ray photoelectron spectroscopy (AR-XPS) was employed to probe the depth-profile of the ultra-thin film grown on FZ-Si. This approach was preferred over sputter-depth profiling, as the latter is well-known to induce artefactual reduction of metal oxides due to ion-induced damage and charging effects [24]. By varying the take-off angles (α), defined as the angle between the sample surface and the electron analyser, different effective sampling depths can be accessed without altering the sample [46]. The sampled depth, d, is given by the Eq. (2):

$$d = 3\lambda \sin\alpha \tag{2}$$

where λ is the inelastic mean free path of the photoelectron within the material.

At α = 90°, where the sample surface is perpendicular to the analyser axis, the maximum sampling depth is reached (i.e., $d = 3\lambda$). As α decreases, the analysis becomes progressively more surface-sensitive. Fig. 4(a) shows the Mo_{3d} XPS spectra acquired at take-off angles ranging from α = 25° to α = 70° for the film deposited on FZ-Si.

The Mo_{3d} line shape remains essentially unchanged for all α values, and the same behaviour is observed for O_{1s} core level (not shown). This invariance indicates that, within the sensitivity limits of AR-XPS (< 1 nm), no appreciable interfacial reduced layer is detected at the MoO_x/Si interface. The Si_{2p} core-level signal was also monitored as a function of α to further assess possible oxidation of the silicon substrate. Fig. 4(b) shows the spectra acquired in the Si_{2p} binding energy region for α values between 25° and 70° While no signal is detected at α = 25°, a distinct signal peaked at 99.4 eV appears at α = 45° and further increases in intensity at α = 70° This signal is attributable to elemental Si^0 from the FZ-Si substrate. No additional components corresponding to oxidized silicon species (e.g. Si^{4+}, Si^{2+}, Si^{3+}) are detected at higher binding energy for any α values. For comparison, Fig. 4(b) also includes the Si_{2p} spectrum acquired from the film grown on SiO_2/FZ-Si substrate at α = 45° In this case, only a peak centred at ~103.4 eV is observed, corresponding to the Si^{4+} oxidation state of thermally grown SiO_2.

Fig. 5 compares the estimated Mo^{6+} fraction, obtained by the Mo_{3d} peak fit, (left axis) together with the normalized Si^0 signal (right axis) as a function of the take-off angle.

Based on literature values of the inelastic mean free path in MoO_x[47–49], $\lambda = 2.5 \pm 0.3$ nm was assumed, yielding an estimated maximum sampling depth of approximately 7.5 nm. It should be noted that these values are derived from models by Seah and Dench or by Tanuma et al. [47,49,50], and experimental deviations of 20–30% from theoretical predictions have been reported [51]. Using this λ value, the effective sampling depths at 25°, 45° and 70° are estimated to be approximately 3.2 nm, 5.3 nm, and 7.0 nm, respectively. Therefore, measurements at lower angle, 25°, provide enhanced surface sensitivity and exclude substrate contributions, whereas higher angles, 45° and 70°, probe the entire film thickness and the MoO_x/Si interface. While the Si^0 signal appears for α ≥ 45° and progressively increases with increasing take-off angle, reflecting the larger effective sampling depth and the growing contribution from the underlying Si substrate, the relative Mo^{6+} fraction remains essentially constant within experimental uncertainty over the entire angular range investigated. These results suggest that no appreciable oxide reduction is detected within the first

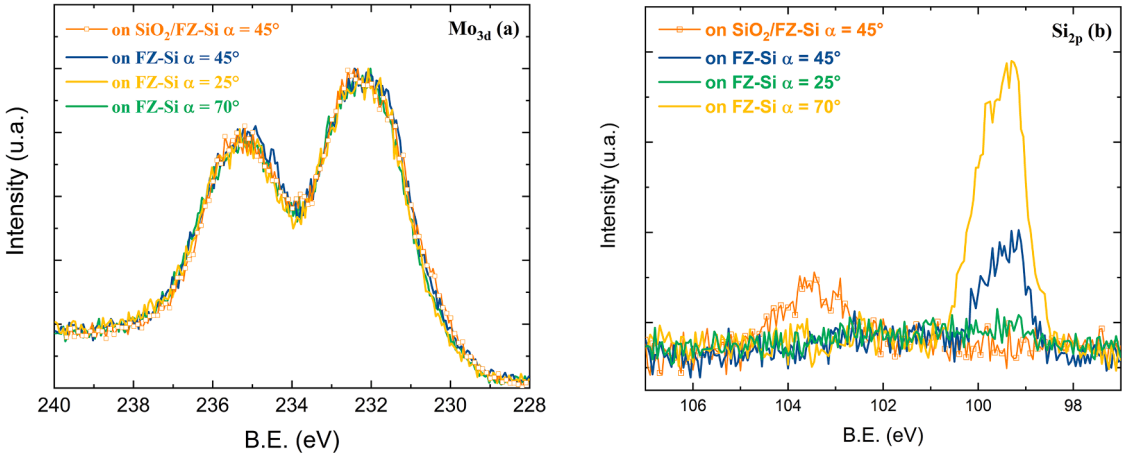


Fig. 4. **(a)** XPS spectra of the Mo_{3d} core level for sputter-deposited molybdenum oxide film grown on SiO_2/FZ-Si substrate, acquired at a take-off angle (α) of 45° For comparison, Mo_{3d} spectra of films deposited on FZ-Si are shown at different α values of 25°, 45° and 70° **(b)** XPS spectra of Si_{2p} core level for molybdenum oxide films grown on FZ-Si, measured at α values of 25°, 45° and 70° For comparison, the Si_{2p} spectrum of the film deposited on SiO_2/FZ-Si substrate is also shown at α = 45°.

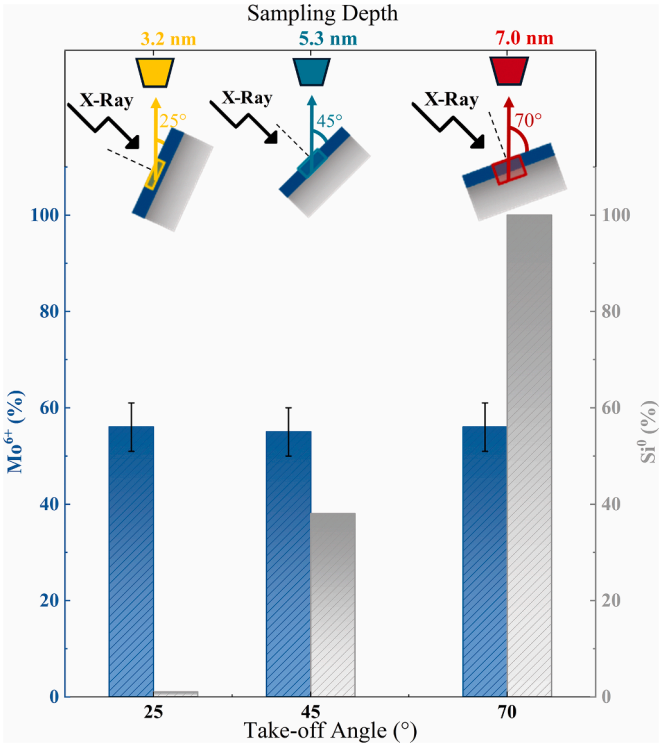


Fig. 5. Angle-resolved XPS analysis of the 5 nm-thick MoO_x film deposited on FZ-Si substrate. Normalized Mo^{6+} peak, extracted from the deconvolution of the Mo_{3d} core-level spectra (left axis), and the normalized Si_{2p} peak (right axis) are reported as a function of the photoelectron take-off angle (α) and sample depth. In the insert a scheme of geometrical configuration at different take-off angles.

nanometers near the MoO_x/Si interface, within the sensitivity limits of AR-XPS.

To probe the MoO_x/Si interface with nanometric resolution, HAADF-STEM measurements were performed, as shown in Fig. 6(a). The HAADF image reveals a uniform MoO_x layer with a thickness of ~5.5 nm, in good agreement with spectroscopic ellipsometry measurements. This is further confirmed by HAADF intensity line profile reported in Fig. 6(c), which indicates a constant signal across the film thickness, consistent with a homogeneous composition.

However, at the same time, a thin amorphous interlayer with a thickness of approximately 1.5–2 nm thick is observed at the MoO_x/Si interface, as highlighted in Fig. 6(a). This interlayer is clearly distinguished by its contrast relative to the adjacent materials and appears comparatively thinner than the interfacial layers commonly reported for thermally evaporated counterparts, which in several studies are found to extend over a thickness of approximately 2–4 nm [52,19,27]. The observed interlayer is most likely attributable to a thin SiO_x layer, originating either from partial reoxidation of the HF-treated FZ-Si surface during the ~10 min air exposure prior to transfer into the sputtering chamber, or from a limited O transfer from the MoO_x film to the FZ-Si substrate. Both phenomena are expected to contribute to the formation of an amorphous interfacial layer. The chemical nature of the interface was further investigated by EDS analysis, reported in Fig. 6(b) and (c). The EDS elemental profiles corroborate the AR-XPS results,

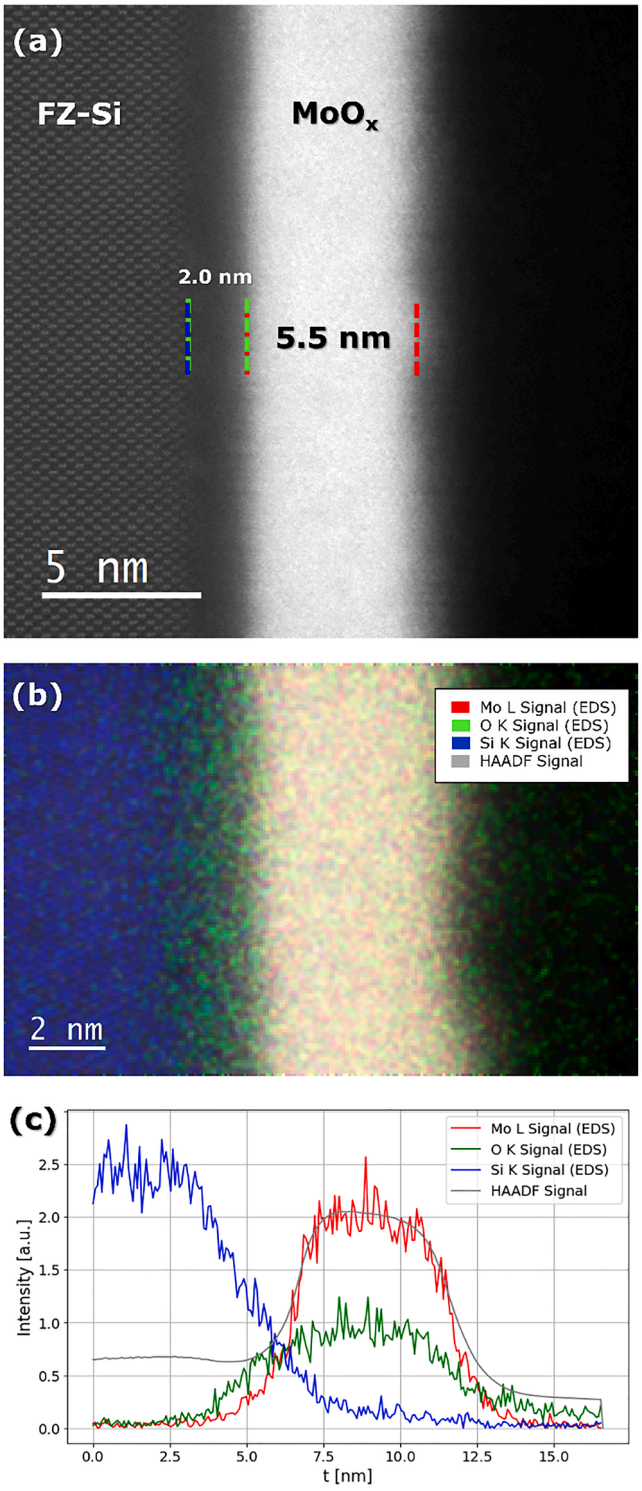


Fig. 6. **(a)** Cross-sectional HAADF-STEM micrograph of the MoO_x/FZ-Si interface, showing the overall film thickness and structural uniformity. An amorphous interface of about 2 nm, attributable to SiO_x, is also highlighted. **(b)** EDS map overlapped to HAADF micrograph and **(c)** elemental and HAADF line profiles acquired across the MoO_x/FZ-Si interface, showing the spatial distribution of Mo, O, Si and HAADF (Z-contrast) signals across the film thickness and the interfacial region.

revealing neither a decrease in the O signal at the onset of the Mo signal nor any variation in the Mo signal across the entire film thickness. This demonstrates that the MoO_x layer preserves a uniform elemental composition up to the near-interface region. The absence of detectable oxygen depletion within the MoO_x film indicates that the observed interlayer does not originate from substrate-induced redox reactions involving MoO_x but is instead associated with the presence of a thin SiO_x layer. Overall, the EDS results confirm the absence of MoO_x reduction at the interface in sputtered films, thus underlying its stability and suggesting that the oxide layer observed is mainly related to an uncontrolled substrate oxidation before deposition.

Thus, the 5 nm-thick sputtered film on Si preserves its stoichiometry throughout the entire thickness, with no evidence of extended interfacial redox reactions, in contrast to what is commonly reported for

thermally evaporated TMOs [19,24,27,45].

This behaviour markedly differs from that reported by Gerling et al. [19] for thermally evaporated V_2O_5 films on Si, where oxide reduction extends to 3–4 nanometers from the SiO_x interlayer, as evidenced by the presence of V^{4+} species generated by $V^{5+}\rightarrow V^{4+}$ reduction. A comparable trend has also been reported for evaporated MoO_3 on Si, where reduced Mo^{5+} states are detected within the first 2–3 nm from the interface and gradually decrease toward bulk-like composition away from the interfacial region [25]. The stoichiometry preservation observed for sputtered films can be rationalized in terms of the distinct deposition kinetics. In thermal evaporation, atoms condense onto the substrate surface with very low kinetic energies, tipically below 1 eV, which may facilitate the activation of interfacial redox reactions due to limited surface mobility and slower film densification [19]. Conversely, sputtered species possess significantly higher kinetic energies, typically in the range of several eV up to ~10 eV[53,54], mainly due to energetic ion bombardment. These conditions are known to promote enhanced two-dimensional surface diffusion, rapid film densification, and high sticking probabilities (>95%), ultimately favouring smooth and compact layer-by-layer growth [55,56]. Such growth conditions can limit the interaction of reactive species with the substrate and are therefore expected to reduce the extent of interfacial reactions [56]. The absence of detectable oxygen depletion and reduced Mo states near the interface observed in this work is consistent with this interpretation.

Overall, sputtering favours the formation of dense and compositionally uniform MoO_x film and is associated with a reduced extent of interfacial reactions compared to low-energy deposition techniques such as thermal evaporation. Altogether, these results underscore the chemical resilience and compositional integrity of sputter-deposited MoO_x ultra-thin films.

Conclusions

This work demonstrates that non-reactive RF magnetron sputtering from a stoichiometric target provides a reliable and scalable route for the growth of 5 nm-thick MoO_x films on silicon. Beyond achieving uniform surface morphology, homogeneous electronic properties with a WF of 5.06 eV, and a stable sub-stoichiometric composition ($x = 2.6$), non-reactive sputtered films exhibit superior compositional integrity on silicon compared to thermally evaporated counterparts, for which extended redox-driven modification is commonly reported. The higher kinetic energy of sputtered species promotes two-dimensional surface diffusion and rapid film densification, thereby limiting substrate-induced interfacial reactions and ensuring chemical robustness even on bare silicon substrates. Collectively, these findings establish non-reactive sputtering as a robust and industrially relevant approach for integrating ultra-thin MoO_x into next-generation electronic, optoelectronic, and photovoltaic devices.

Supporting information

The following files are available free of charge.

Notes

The authors declare no competing financial interests.

CRediT authorship contribution statement

Salvatore La Manna: Writing – review & editing, Writing – original draft, Visualization, Methodology, Investigation, Formal analysis, Data curation. **Vanna Torrisi:** Writing – review & editing, Visualization, Investigation, Formal analysis, Data curation. **Giorgia Franzò:** Writing – review & editing, Visualization, Validation, Methodology. **Cristiano Lo Pò:** Visualization, Investigation, Formal analysis. **Elisa Brugaletta:** Writing – review & editing, Investigation, Formal analysis, Data curation. **Antonio Massimiliano Mio:** Writing – review & editing, Validation, Investigation, Formal analysis, Data curation. **Antonio Terrasi:** Writing – review & editing, Visualization, Validation, Supervision, Methodology. **Guglielmo G. Condorelli:** Writing – review & editing, Visualization, Investigation. **Maria Miritello:** Writing – review & editing, Visualization, Validation, Supervision, Project administration, Data curation, Conceptualization.

Declaration of competing interest

The authors declare that they have no known competing financial interests or personal relationships that could have appeared to influence the work reported in this paper.

Acknowledgements

The research was funded by Italian Project PNRR “Sicilian Micro-nanoTech Research and Innovation Center” (SAMOTHRACE), Ecosistema dell’Innovazione, grant number ECS00000022, CUP B63C22000620005. The authors thank also the C.2 – Horizon Europe Energy Project FreeHydroCells (G.A. n.101084261) and Bionanotech Research and Innovation Tower (BRIT) laboratory of University of Catania (Grant no. PONa3_00136 financed by the Italian Ministry for Education, University and Research, MIUR) for the XPS facility. A. Terrasi acknowledges the financial support of the project GOPV (Materiali di nuova GenerazIOne Per celle fotoVoltaiche tandem), financed by MASE (formerly MITE) – System Research Call - CSEA - TYPE A, of the Ministry of Ecological Transition. A. M. Mio and E. Brugaletta acknowledge financial support by the project, BEYOND NANO Upgrade (CUP G66J17000350007) and by NextGenerationEU, M4C2, within the PNRR project NFFA—DI, CUP B53C22004310006, IR0000015, having benefited from the access provided by CNR−IMM@CT in Catania. Authors acknowledge the Laboratory of Quantum Technologies at Department of Physics and Astronomy of the University of Catania. C. Percolla and G. Pantè are greatly acknowledged for their expert technical support.

Supplementary materials

Supplementary material associated with this article can be found, in the online version, at doi:10.1016/j.oceram.2026.100978.

References

[1] S. Feng, B. Li, B.O. Xu, Z. Wang, Hybrid perovskites and 2D materials in optoelectronic and photocatalytic applications, Crystals 13 (2023) 1566, https://doi.org/10.3390/cryst13111566.

[2] A.A Odebowale, A.M Berhe, D. Somaweera, H. Wang, W. Lei, A.E. Miroshnichenko, H.T. Hattori, Advances in 2D photodetectors: materials, mechanisms, and applications, Micromachines 16 (2025) 776, https://doi.org/10.3390/mi16070776.

[3] A.V. Juan-Arturo, A. Leonel Mendoza-Martínez, G. Morales-Luna, M. Morales-Luna, Exploring the optical properties of molybdenum trioxide: approach of theory modeling and depositions techniques, Adv. Phys. X. 10 (2025) 1–34, https://doi.org/10.1080/23746149.2025.2451687. No.01.

[4] A. Mohamed, M.A.L.-D. Basyooni, E. Shrouk, Y.RE. Zaki, M. Yilmaz, S. Mohamed, Tuning the metal–Insulator transition properties of VO_2 thin films with the synergetic combination of oxygen vacancies, strain engineering, and tungsten doping, Nanomaterials 12 (2022) 1470, https://doi.org/10.3390/nano12091470.

[5] A.V. Avani, E.I. Anila, Recent advances of MoO_3 based materials in energy catalysis: applications in hydrogen evolution and oxygen evolution reactions, Int. J. Hydrog. Energy 47 (47) (2022) 20475–20493, https://doi.org/10.1016/j.ijhydene.2022.04.252.

[6] B. Jansi Rani, G. Ravi, R. Yuvakkumar, F. Ameen, S. AlNadhari, S.I. Hong, Fabrication and electrochemical OER activity of Ag doped MoO_3 nanorods, Mater. Sci. Semicond. Process. 107 (2020) 104818, https://doi.org/10.1016/j.mssp.2019.104818.

[7] S. La Manna, G. Franzò, A. Terrasi, G.G. Condorelli, M. Miritello, Stoichiometry modulation of molybdenum oxide thin films by direct sputtering for energy applications, Surf. Coat. Technol. 496 (2025) 131663, https://doi.org/10.1016/j.surfcoat.2024.131663.

[8] W. Li, J. Shi, K.H.L. Zhang, J.L. MacManus-Driscoll, Defects in complex oxide thin films for electronics and energy applications: challenges and opportunities, Mater. Horiz. 7 (2020) 2832–2859, https://doi.org/10.1039/D0MH00899K.

[9] M.T. Greiner, M.G. Helander, T. Wing-Man, Z.-B. Wang, J. Qiu, Z.-H. Lu, Universal energy-level alignment of molecules on metal oxides, Nat. Mater. 11 (2012) 76–81, https://doi.org/10.1038/nmat3159.

[10] M. Morales-Luna, S.A. Tomàs, M.A. Arvizu, M. Pérez-Gonzàlez, E. Campos-Gonzalez, The evolution of the Mo^{5+} oxidation state in the thermochromic effect of MoO_3 thin films deposited by rf magnetron sputtering, J. Alloys. Compd. 722 (2017) 938–945, https://doi.org/10.1016/j.jallcom.2017.06.149.

[11] T.S. Sian, G.B. Reddy, Optical, structural and photoelectron spectroscopic studies on amorphous and crystalline molybdenum oxide thin films, Sol. Energy Mater. Sol. Cells 82 (2004) 375–386, https://doi.org/10.1016/j.solmat.2003.12.007.

[12] T.V. Sviridova, L.Y.U. Sadovskaya, E.M. Shchukina, A.S. Logvinovich, D. G. Shchukin, D.V. Sviridov, Nanoengineered thin-film TiO_2/h-MoO_3 photocatalysts capable to accumulate photoinduced charge, J. Photochem. Photobiol. A: Chem. 327 (2016) 44–50, https://doi.org/10.1016/j.jphotochem.2016.04.018.

[13] W. Marchal, I. Verboven, J. Kesters, B. Moeremans, C. De Dobbelaere, G. Bonneux, K. Elen, B. Conings, W. Maes, H.G. Boyen, W. Deferme, M. Van Bael, A. Hardy, Steering the properties of MoO_x hole transporting layers in OPVs and OLEDs: interface morphology vs. Electronic structure, Materials 10 (2017) 123, https://doi.org/10.3390/ma10020123.

[14] L.G. Gerling, S. Mahato, A. Morales-Vilches, G. Masmitja, P. Ortega, C. Voz, R. Alcubilla, P. Joaquim, Transition metal oxides as hole-selective contacts in silicon heterojunctions solar cells, Sol. Energy Mater. Sol. Cells 145 (2016) 109–115, https://doi.org/10.1016/j.solmat.2015.08.028.

[15] Y. Wang, S.-T. Zhang, L.I. Le, X. Yang, L. Lu, D. Li, Dopant-free passivating contacts for crystalline silicon solar cells: progress and prospects, EcoMat 5 (2023) e12292, https://doi.org/10.1002/eom2.12292.

[16] B. Roose, Q. Wang, A. Abate, The role of charge selective contacts in Perovskite solar cell stability, Adv. Energy Mater. 9 (2019) 1803140, https://doi.org/10.1002/aenm.201803140.

[17] K. Singh, M. Nayak, D. Kumar Singh, V.K. Komarala, Degradation study of carrier selective contact silicon solar cells with ageing: role of silicon surface morphology, Solid. State Electron. 179 (2021) 107987, https://doi.org/10.1016/j.sse.2021.107987.

[18] J. Kumari, J. Shree Bhardwaj, Rahul, P. Agarwal, Oxygen plasma treatment of thermally evaporated MoO_{3-x} films: an approach to tune the work function, ACS Appl. Electron. Mater. 5 (2023) 4103–4113, https://doi.org/10.1021/acsaelm.3c00343.

[19] L.G. Gerling, C. Voz, R. Alcubilla, J. Puigdollers, Origin of passivation in hole-selective transition metal oxides for crystalline silicon heterojunction solar cells, J. Mater. Res. 32 (2) (2017) 260–268, https://doi.org/10.1557/jmr.2016.453.

[20] G. Du, L.E. Li, X. Yang, X.I. Zhou, Z. Su, P. Cheng, Y. Lin, L. Lu, J. Wang, L. Yang, X. Gao, X. Chen, D. Li, Improved V_2O_x passivating contact for p-type crystalline silicon solar cells by oxygen vacancy modulation with a SiO_x tunnel layer, Adv. Mater. Interfaces. 8 (2021) 2100989, https://doi.org/10.1002/admi.202100989.

[21] Irfan, H. Ding, Y. Gao, C. Small, D.O.Y. Kim, J. Subbiah, F. So, Energy level evolution of air and oxygen exposed molybdenum trioxide films, Appl. Phys. Lett. 96 (2010) 243307, https://doi.org/10.1063/1.3454779.

[22] I. Irfan, A.J Turinske, Z. Bao, Y. Gao, Work function recovery of air exposed molybdenum oxide thin films, Appl. Phys. Lett. 101 (2012) 093305, https://doi.org/10.1063/1.4748978.

[23] K. Trzciński, Z. Zarach, M. Szkoda, A.P. Nowak, K. Berent, M.ł Sawczak, Controlling crystallites orientation and facet exposure for enhanced electrochemical properties of polycrystalline MoO_3 films, Sci. Rep. 13 (2023) 16668, https://doi.org/10.1038/s41598-023-43800-9.

[24] J. Tong, T.T. Le, W. Liang, M.D.A. Hossain, K.R. McIntosh, P. Narangari, S. Armand, T.C. Kho, K.T. Khoo, Y. Zakaria, A.A. Abdallah, S. Surve, M. Ernst, B. Hoex, K.C Fong, Impact of pre-grown SiO_x on the carrier selectivity and thermal stability of molybdenum-oxide-passivated contact for Si solar cells, ACS. Appl. Mater. Interfaces. 13 (2021) 36426–36435, https://doi.org/10.1021/acsami.1c06765.

[25] L.G. Gerling, S. Mahato, C. Voz, R. Alcubilla, P. Joaquim, Characterization of transition metal oxide/silicon heterojunctions for solar cell applications, Appl. Sci. 5 (2015) 695–705, https://doi.org/10.3390/app5040695.

[26] D. Sacchetto, Q. Jeangros, G. Christmann, L. Barraud, A. Descoeudres, J. Geissbühler, M. Despeisse, A. Hessler-Wyser, S. Nicolay, C. Ballif, ITO/MoO_x/a-Si:h(i) hole-selective contacts for silicon heterojunction solar cells: degradation mechanisms and cell integration, in: IEEE Journal of Photovoltaics 7, 2017, pp. 1584–1590, https://doi.org/10.1109/JPHOTOV.2017.2756066.

[27] T. Zhang, C.-Y. Lee, Y. Wan, S. Lim, B. Hoex, Investigation of the thermal stability of MoO_x as hole-selective contacts for Si solar cells, J. Appl. Phys. 124 (2018) 073106, https://doi.org/10.1063/1.5041774.

[28] W.D. Westwood, Sputter deposition processes, MRS Bull. 13 (1988) 46–51, https://doi.org/10.1557/S0883769400063697.

[29] S. Krishna, Chapter 7 - Sputter Processing Pages 195-230. ISBN: 978-0-12-812311-9, Handbook of Thin Film Deposition - Fourth Edition, 2018, https://doi.org/10.1016/C2016-0-03243-6.

[30] S. Goetz, R.A Wibowo, M. Bauch, N. Bansal, G. Ligorio, E. List-Kratochvil, C. Linke, E. Franzke, J. Winkler, M. Valtiner, T. Dimopoulos, Fast sputter deposition of MoO_x/metal/MoO_x transparent electrodes on glass and PET substrates, J. Mater. Sci. 56 (2021) 9047–9064, https://doi.org/10.1007/s10853-021-05839-9.

[31] P.K. Parashar, V.K. Komarala, Sputter deposited sub-stochiometric MoOx thin film as hole-selective contact layer for silicon based heterojunction devices, Thin. Solid. Films. 682 (2019) 76–81, https://doi.org/10.1016/j.tsf.2019.05.004.

[32] I.D. Baikie, A.C. Grain, J. Sutherland, J. Law, Ambient pressure photoemission spectroscopy of metal surfaces, Appl. Surf. Sci. 323 (2014) 45–53, https://doi.org/10.1016/j.apsusc.2014.08.159.

[33] S. Bhatia, I.M. Khorakiwala, P.R. Nair, A. Antony, Influence of post deposition fabrication steps and quantitative estimation of band diagram of Si/MoO_X heterojunction for carrier selective solar cells, Sol. Energy 194 (2019) 141–147, https://doi.org/10.1016/j.solener.2019.10.025.

[34] D. Kang, H.-S. Lee, D. Kim, Y. Kang, Investigation of sub-stoichiometric MoO_x hole-selective contacts for rear junction passivating contact silicon solar cells, J. Sci.: Adv. Mater. Devices 9 (2024) 100647, https://doi.org/10.1016/j.jsamd.2023.100647, 093305.

[35] M. Ponce-Mosso, M. Pérez-González, P.E. García-Tinoco, H. Crotte-Ledesma, M. Morales-Luna, S.A. Tomás, Enhanced photocatalytic activity of amorphous MoO3 thin films deposited by rf reactive magnetron sputtering, Catal. Today 349 (2020) 150–158, https://doi.org/10.1016/j.cattod.2018.04.065.

[36] L. Zhu, R. Miao, T.D Huan, I.M. Mosa, A.S. Poyraz, Z. Wei, J.E. Cloud, D.A. Kriz, S. Thanneeru, J. He, Y. Zhang, R. Ramprasad, S.L. Suib, Mesoporous MoO_{3-x} material as an efficient electrocatalyst for hydrogen evolution reactions, Adv. Energy Mater. 6 (2016) 1600528, https://doi.org/10.1002/aenm.201600528.

[37] L. Xiaxia, A.H.R. Jeong, R.G. Wilks, S. Wiesner, M. Rusu, R. Félix, X. Ting, C. Hartmann, M. Bär, Tunability of MoO_3 thin-film properties due to annealing in situ monitored by hard X-ray photoemission, ACS. Omega 4 (2019) 10985–10990, https://doi.org/10.1021/acsomega.9b01027.

[38] K. Inzani, M. Nematollahi, S.M. Selbach, T. Grande, F. Vullum-Bruer, Progression of reduction of MoO3 observed in powders and solution-processed films, Thin. Solid. Films. 626 (2017) 94–103, https://doi.org/10.1016/j.tsf.2017.02.029.

[39] S.Q Hussain, K. Mallem, Y.J Kim, A.HT. Le, M.Q Khokhar, S. Kim, S. Dutta, S. Sanyal, Y. Kim, J. Park, Y. Lee, Y.H Cho, E.C Cho, J. Yi, Ambient annealing influence on surface passivation and stoichiometric analysis of molybdenum oxide layer for carrier selective contact solar cells, Mater. Sci. Semicond. Process. 91 (2019) 267–274, https://doi.org/10.1016/j.mssp.2018.11.028.

[40] B.Y Zhang, A. Zavabeti, A.F. Chrimes, F. Haque, L.A. O'Dell, H. Khan, N. Syed, R. Datta, Y. Wang, A.S.R. Chesman, T. Daeneke, K. Kalantar-zadeh, J.Z Ou, Degenerately hydrogen doped molybdenum oxide nanodisks for ultrasensitive plasmonic biosensing, Adv. Funct. Mater. 28 (2018) 1706006, https://doi.org/10.1002/adfm.201706006.

[41] A.A. Mane, A.V. Moholkar, Orthorhombic MoO_3 nanobelts based NO_2 gas sensor, Appl. Surf. Sci. 405 (2017) 427–440, https://doi.org/10.1016/j.apsusc.2017.02.055.

[42] M. Sendova-Vassileva, H.R. Dikov, P. Vitanov, G. Popkirov, R. Gergova, G. Grancharov, V. Gancheva, Magnetron sputtered molybdenum oxide for application in polymers solar cells, J. Phys.: Conf. Ser. 764 (2016) 012022, https://doi.org/10.1088/1742-6596/764/1/012022.

[43] C.D. Wagner, L.E. Davis, M.V. Zeller, J.A. Taylor, R.H. Raymond, L.H. Gale, Empirical atomic sensitivity factors for quantitative analysis by electron spectroscopy for chemical analysis, Surf. Int. Anal. 3 (1981) 211–225.

[44] J.W. Coburn, E. Taglauer, E. Kay, A study of the neutral species rf sputtered from oxide targets, J. Appl. Phys. 13 (1974) 501.

[45] M. Gao, C. Dongyun, B. Han, W. Song, M. Zhou, X. Song, F. Xu, L. Zhao, Y. Li, Z. Ma, Bifunctional hybrid a-SiO_x(Mo) layer for hole-selective and interface passivation of highly efficient MoO_x/a-SiO_x(Mo)/n-Si heterojunction photovoltaic device, ACS. Appl. Mater. Interfaces. 10 (2018) 27454–27464, https://doi.org/10.1021/acsami.8b07001.

[46] D.B Cumpson, J.T. Grant, Angle-resolved X-ray photoelectron spectroscopy. Surface Analysis by Auger and X-ray Photoelectron Spectroscopy, Surface Spectra Limited. Manchester, 2003.

[47] A. Galtayries, S. Wisniewski, J. Grimblot, Formation of thin oxide and sulphide films on polycrystalline molybdenum foils: characterization by XPS and surface potential variations, J. Electron. Spectros. Relat. Phenom. 87 (1997) 31–44, https://doi.org/10.1016/S0368-2048(97)00071-6.

[48] Y.L. Leung, P.C. Wong, K.A.R. Mitchell, K.J. Smith, X-ray photoelectron spectroscopy studies of the reduction of MoO_3 thin films by NH_3, Appl. Surf. Sci. 136 (1998) 147–158, https://doi.org/10.1016/S0169-4332(98)00341-9.

[49] M.P. Seah, W.A. Dench, Quantitative electron spectroscopy of surfaces: a standard data base for electron inelastic mean free paths in solids, Surf. Interface Anal. 1 (1) (1979) 2–11. No.

[50] S. Tanuma, S.J. Powell, D.R. Penn. Surf. Interface Anal. 11 (1988) 577.

[51] E. Minni, F. Werfel, Oxygen interaction with Mo(100) studied by XPS, AES and EELS, Surf. Interface Anal. 12 (1988) 385–390, https://doi.org/10.1002/sia.740120704.

[52] H. Ali, C.é Maynau, L. Lajaunie, G. Gregory, L. Wu, J.P Looney, Y. Zhu, M. Schneider, W.V. Schoenfeld, K.O. Davis, Transmission electron microscopy and electron energy-loss spectroscopy studies of hole-selective molybdenum oxide

contacts in silicon solar cells, ACS. Appl. Mater. Interfaces. 11 (2019) 43075–43080, https://doi.org/10.1021/acsami.9b12703.
[53] NastjaMahne, M. Cekada, M.ž Panjan, Energy distribution of sputtered atoms explored by SRIM simulations, Coatings 13 (2023) 1448, https://doi.org/10.3390/coatings13081448.
[54] J. Lu, C.G Lee, Numerical estimates for energy of sputtered target atoms and reflected Ar neutrals in sputter processes, Vacuum 86 (2012) 1134–1140, https://doi.org/10.1016/j.vacuum.2011.10.018.
[55] R. Garg, S. Gonuguntla, S. Sk, M. Saqlain Iqbal, A. Oluwasogo Dada, U. Pal, M. Ahmadipour, Sputtering thin films: materials, applications, challenges and future directions, Adv. Colloid. Interface Sci. 330 (2024) 103203, https://doi.org/10.1016/j.cis.2024.103203.
[56] G. Zhu, M. Han, B. Xiao, Z. Gan, Influence of sputtering pressure on the micro-topography of sputtered Cu/Si films: integrated multiscale simulation, Processes 11 (2023) 1649, https://doi.org/10.3390/pr11061649.